ACS Photonics

Article

pubs.acs.org/journal/apchd5

Narrow Collective Plasmon Resonances in Nanostructure Arrays Observed at Normal Light Incidence for Simplified Sensing in Asymmetric Air and Water Environments

Benjamin D. Thackray,*[,†] Vasyl G. Kravets,[†] Fred Schedin,[†] Gregory Auton,[‡] Philip A. Thomas,[†] and Alexander N. Grigorenko[†]

[†]School of Physics and Astronomy and [‡]School of Computer Science, The University of Manchester, Manchester, M13 9PL, United Kingdom

ABSTRACT: We fabricate gold plasmonic nanoarrays on a glass substrate supporting narrow collective (diffraction coupled) resonances that can be excited with normal incident light in an asymmetric air or water environment. We measure quality factors of normal incidence resonances up to 19 in air, 45 in water, and 85 in glycerol and register a very high figure of merit for biosensing applications in water. The coupled dipole approximation is used to evaluate the optimum resonance conditions and qualitatively explain the properties of the resonances. Our results could help to develop simpler and cheaper surface plasmon resonance based approaches to gas and biodetection.

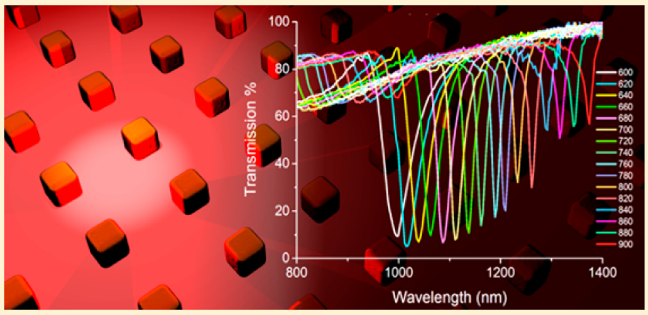

KEYWORDS: *biosensing, coupled, plasmon, resonances, nanoarray, nanoparticles, figure-of-merit*

Surface plasmon resonance (SPR) is a well-established technique for detecting trace amounts of adsorbents at an interface. SPR sensors typically use the Kretschmann configuration to excite propagating surface plasmon modes at the interface between a thin metal film and dielectric medium. The technique is fast and highly sensitive. For example, both proteins,[1] such as insulin,[2] and DNA[3] can be detected at nanomolar (nM) concentrations. SPR-based sensing is a major application of plasmonics, and several companies offer commercial devices.[4,5] However, commercial devices based on the Kretschmann configuration have a number of disadvantages. A high-quality gold film, steep angle of incidence (AOI), and a prism are required to enable light to couple to the higher momentum SPR modes. As a result, the apparatus and consumables for SPR-based detection are quite expensive.[4,6] Sensor chips based on gold slides cannot normally be reused and may not allow high-throughput analysis. A 2008 general review of biosensors[4] emphasizes the significance of technique accessibility as a limiting factor for the adoption of sensing technologies. Additional limitations of SPR are that detection is limited to one specific SPR wavelength and the sensing area is not strongly localized on the sample surface.

If light can be strongly coupled to plasmon resonances at normal incidence, then detection can be performed in a standard microscope without specialist optics, making it much more accessible. Even if detection sensitivity is lower than commercial apparatus, this factor, coupled with the potential for additional novel functionalities provided by non-SPR methods, could still open up the technology for applications where extreme sensitivity is unnecessary.[6]

Localized surface plasmon resonances (LSPRs) in subwavelength metallic nanostructures provide a solution to some of SPR's limitations.[7] LSPR-based detection can usually be performed at normal incidence and can also provide nanometer-scale surface localization. Additionally, the LSPR wavelength can be tuned from the visible and into the infrared by variation of the nanostructure geometry.

LSPR resonances in simple isolated structures tend to be spectrally broad and of low quality factor, but very high detection sensitivities have been achieved with novel structures. For example, neurotoxins linked to Alzheimer's disease have been detected at ∼100 fM concentrations on a substrate made with nanosphere lithography.[7,8] Overall, LSPR could offer sensitivity comparable to commercial devices, but could also be cheaper and offer higher spatial resolution and a tunable resonance wavelength[9] especially in phase interrogation.[10]

Interactions between nearby plasmonic nanostructures can create hybrid modes that significantly improve their suitability for biosensing applications.[11] Our results fall into this category, exploiting an effect known as "collective resonances" or "diffraction coupling".[12−15] Diffraction coupling occurs when nanostructures are spaced so that the scattered field from each structure arrives in phase with the electron oscillations in its neighbors. The scattered light is then recaptured as electron oscillation, reducing energy loss to the far field and retaining it as plasmon resonance, thereby increasing the resonance quality

Received: June 17, 2014
Published: October 24, 2014

dx.doi.org/10.1021/ph5002186 | *ACS Photonics* 2014, 1, 1116−1126

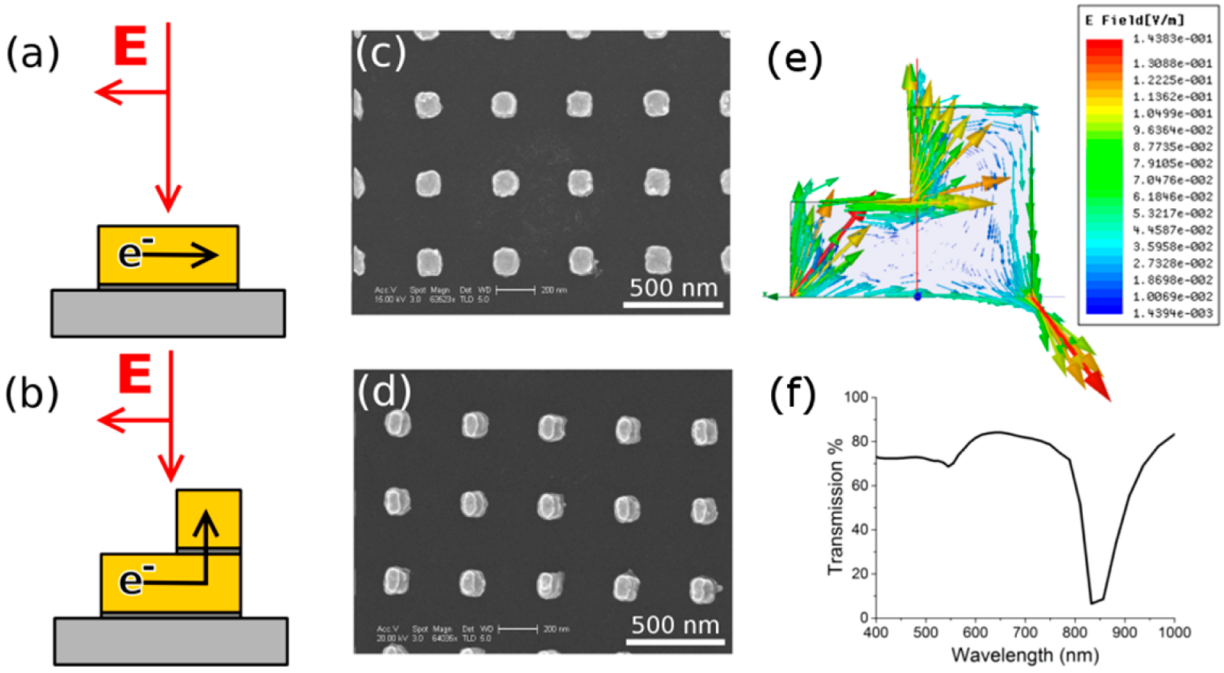

Figure 1. Cross-sectional side view of nanostructures, SEM images, and FDTD simulation. (a) Cross-sectional diagram of a square nanostructure fabricated with one lithography step. (b) Cross-sectional diagram of an L-shaped nanostructure fabricated with two lithography steps. (c) SEM image of an array of square structures with period 400 nm. (d) SEM image of an array of L-shaped structures with period 400 nm. (e) FDTD simulation of 150 nm L-shapes in an array of period 544 nm. (f) Predicted transmission spectrum from the FDTD simulation. The diagrams (a and b) depict the structures after etching of chromium from the substrate (though the Cr adhesion layers from each gold deposition remain), while the SEM images (c and d) were taken before the chromium etch, to avoid charging. (a) and (b) depict the incident electric field at normal incidence, and the expected electron motion it will produce. Lines of 200 μm long (y-direction) with the same (x, z) profiles depicted in (a) and (b) were also fabricated, but produced few interesting results.

factor. Phase-based approaches exploiting this effect can achieve sensitivities up to the fg/mm^2 level.[16] Typically these diffraction-coupled resonances are excited only at a steep AOI around ~60°,[13] although in arrays of tall nanostructures, narrow resonances in a symmetric environment have been attained at shallower angles, such as 15°.[17] These results were attributed to the out-of-plane coupling of the localized surface plasmon resonances of the individual nanostructures, facilitated by the tall nanostructures. Diffraction coupled resonances at normal incidence have been predicted and measured[14] in arrays of gold nanospheres, but strong resonances are typically only observed in an index-matched environment. Auguié et al. explain in a theoretical study of the dipolar model how an asymmetric environment can suppress the collective resonance modes in an array, especially in the case of structures that are small compared to their period. They go on to predict that this could be overcome with larger or asymmetric nanostructures, a prediction that we confirm. Excitation of collective resonances in arrays at normal incidence has been presented from a water/glass asymmetric environment,[18] but not to our knowledge from an environment as asymmetric as the air/glass environment.

Here we present gold nanostructure arrays that have high quality factor resonances at normal incidence in air, water, and glycerol and novel resonance modes in asymmetric, L-shaped nanostructures that were also observed. We have measured near-infrared resonance quality factors as high as 19 in air (spectral position 843 nm), 45 in water (1025 nm), and 85 in glycerol (1228 nm). The LSPR of nanoparticles when the collective mode was not excited had quality Q = 9 in air in the red part of the spectrum.

EXPERIMENTAL RESULTS

To achieve collective resonances at normal incidence, one needs to use either composite or large nanostructures as an array elementary cell. Composite nanostructures show strong near-field coupling inside the nanostructure[19,20] that alleviates restrictions imposed on the plasmon resonance of a simple sphere, while large nanostructures demonstrate the small absorption necessary for existence of the normal angle resonance (see the Theory section).

First, we studied composite nanostructures for realization of normal-angle collective resonances, fabricating the "L"-shaped structures shown in Figure 1b,d. Our reasoning was as follows: normal incident light will excite in-plane electron resonance in the base of the L-shaped structure, which is electrically connected to the out-of-plane stem of the L-shaped structure. The in-plane electron oscillation induced in the base by the incident light should then drive out-of-plane electron oscillation in the stem, coupling the normally incident light to the collective out-of-plane modes of the array. Figure 1 illustrates the principle behind the design. FDTD simulation predictions supported our expectations, as shown in Figure 1e,f.

The structures were fabricated from gold on a glass substrate by electron beam lithography. The first arrays were 200 μm × 200 μm overall, with periods of 400 and 500 nm. Square nanostructures 130 nm × 130 nm and 80 nm tall were fabricated in the first lithographic step. Then a second lithographic step added the second layer of 130 nm × 60 nm, 60 nm tall gold to the top of each structure to complete the out-of-plane L-shapes (e.g., Figure 1d). Each array of squares was created with a duplicate control array in the first lithographic step, which was left untouched by the second

dx.doi.org/10.1021/ph5002186 | ACS Photonics 2014, 1, 1116−1126

lithography. A 3 nm chromium adhesion layer was first evaporated beneath each layer of gold deposited, as well as over the entire glass substrate, to prevent charging during electron beam lithography. The chromium layer was later etched from the glass substrate, as at normal incidence the metallic sublayer can effectively suppress plasmonic resonance due to resistive coupling.[21,22] The resulting structures can be seen in the SEM images in Figure 1: Figure 1c shows an array of simple squares, and Figure 1d shows an array of out-of-plane L-shapes.

Figure 2 shows the transmission spectra measured for these nanoarrays. At normal incidence, the L-shaped structures failed

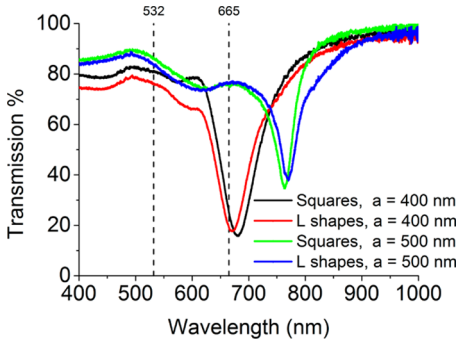

Figure 2. Transmission at normal incidence for 400 and 500 nm period arrays of square and L-shaped nanostructures in water. Vertical lines indicate the position of the Rayleigh anomalies at normal light incidence.

to exhibit any significant improvement on the control samples in air or water (Figure 2). However, ellipsometry (Figure 3) demonstrated some significant differences. Ellipsometry characterizes sample optical properties via the ellipsometric parameters Ψ and Δ, where $\tan(\Psi)\exp(i\Delta) = r_p/r_s$, and r_p and r_s are the amplitude reflection coefficients for p- and s-polarized light, respectively. Because ellipsometry measures the ratio of the reflection coefficients, it is immune to noise caused by random fluctuation, e.g., in the source light intensity. Both squares and L-shapes demonstrate the familiar[13] diffraction-coupled resonance at a high angle of incidence (60−65°). At the same time, the L-shaped structures demonstrate a significantly stronger resonance than the squares at shallower angles of incidence (45−55°). Transmission results at an angle (Figure 4) also show a distinction between the L-shapes and squares. For small (5−25°) angles of incidence, the two structures behave similarly. However, at higher angles of incidence the resonance quality decreases significantly for the square structures, while the L-shapes retain the quality of their resonances up to 40°, above which they also decrease in strength, until 55−60°, where the transmission minimum becomes deeper again. Both structures show a similar blue-shift of approximately 20−25 nm of the resonance position as the angle increases from 5° to 60°. The blue-shift is stronger at smaller angles of incidence.

Unfortunately, the novel resonances in the L-shaped structures were excited too far from normal incidence for our intended biosensing application. At normal incidence, the L-shapes provide no improvement on simple square structures, which suggests that coupling to the out-of-plane mode is difficult to achieve under normal illumination. More positively, the resonances in the arrays of square structures were surprisingly good, especially considering the adverse effect that asymmetric environments can have on resonances at normal incidence.[15] The reason for the limited success of the L-shaped structures lies in strong absorption observed in a unit cell of the structure. We found that larger nanostructures (which show smaller absorption and larger scattering) were more suitable for excitation of normal angle collective resonances.

Building on these results, we decided to optimize the diffractive coupled resonance observed in regular arrays of simple square nanostructures. We fabricated a set of arrays with a larger variety of periods and square sizes using the same fabrication procedure as for the previous structures, but without a second lithography step. The square height was 80 nm, and again the chromium layer was etched from the substrate after fabrication and SEM imaging. From the variety of square sizes on this sample (120 nm, 140 nm, 160 nm) we have presented just the results from squares 160 nm in size, which showed the best resonances overall (Figure 5d shows the effect of the square size on the resonances of an array with period 450 nm, confirming of the importance of the nanostructure size).[15] Figure 5 displays selected transmission results from the new samples in air, water, and glycerol. Good resonances exist in glycerol (expected, as the environment is symmetric), but more unusually also in water and air (especially for the sample with 400 nm period).

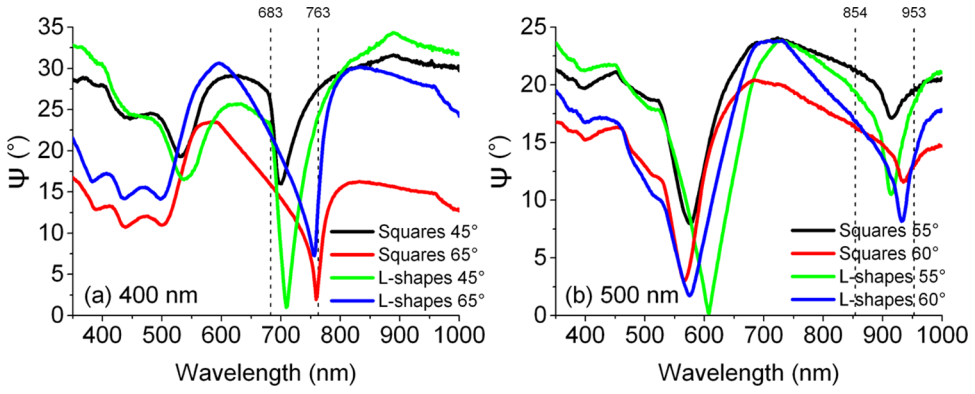

Figure 3. Ellipsometry of square and L-shaped nanostructure arrays. (a) Array period 400 nm. (b) Array period 500 nm. While the behavior of both structures is similar for the well-documented diffraction-coupled resonance excited at around 60°,[13] the behavior of squares and L-shapes differs significantly at shallower angles, with the L-shapes exhibiting a second resonance at 45° when a = 400 nm and at 55° when a = 500 nm (green lines). Vertical lines indicate the position of the air Rayleigh anomalies.

dx.doi.org/10.1021/ph5002186 | ACS Photonics 2014, 1, 1116−1126

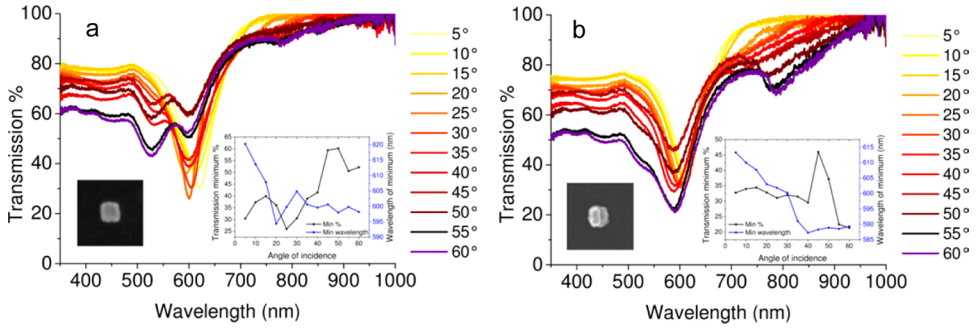

Figure 4. Transmission for angles of incidence from 5° to 60° (a) for square nanostructures with period 400 nm and (b) for L-shaped nanostructures with period 400 nm. Insets show an SEM image of a typical nanostructure and plot the depth and spectral position of the local minimum at ~600 nm. While the squares have a sharper minimum, the transmission minimum remains deep at higher angles for the L-structures. Both structures exhibit a similar blue-shift of the resonance wavelength with increasing angle.

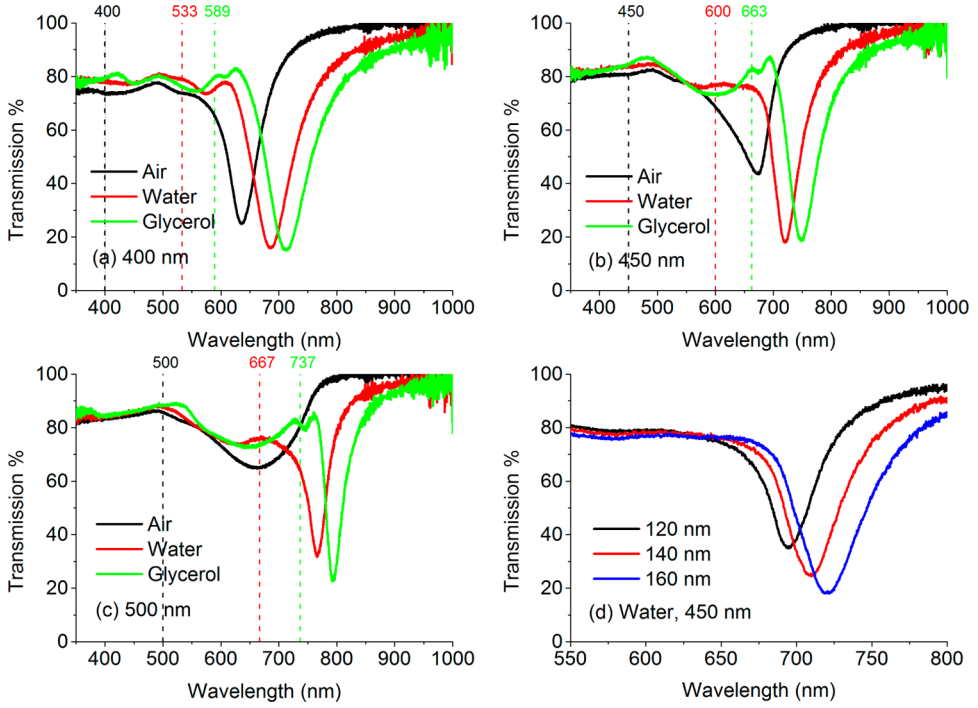

Figure 5. Transmission from arrays of square nanostructures in air, water, and glycerol. (a) Transmission of an array with period 400 nm (b) Transmission of an array with period 450 nm (c) Transmission of an array with period 500 nm. (d) Close-up of minimum transmission from arrays with nanostructures of different sizes with period 450 nm in water. Vertical lines indicate the calculated position of the Rayleigh anomaly at normal incidence.

To further improve our normal incidence resonances, we turned to the coupled dipole model of Markel[23] and Schatz[24] (see Theory section) and attempted to use it as an approximate theoretical model to predict optimal combinations of array period and nanostructure size. Figure 6a–c shows the predicted maximum extinction (per particle) in air, water, and glycerol environments, as a function of nanostructure (assumed spherical) radius and period (100 nanostructures simulated; we later considered the effect of spatial coherence when using focusing optics in d–f). It is clear that optimal combinations lie on or close to the dotted lines indicated. The lines could be approximately fitted to give equations for optimal radius of nanostructure $r = (a/6.30) - 28$ in air, $r = (a/6.15) - 20$ in water, and $r = (a/6.35) - 15$ in glycerol, where a is array period. These results also suggest that nanostructures that are slightly larger than optimal for a given period perform better than those that are slightly smaller.

From this, we designed and made square nanoarrays (methods as before) with larger nanostructures, dimensions around 200 nm × 200 nm (in-plane) × 100 nm (out-of-plane), with periods from 600 to 900 nm, in steps of 20 nm. The results from these samples were disappointing in air, showing no good resonances (not presented), but well-behaved in water and glycerol (Figure 7), demonstrating high quality factor resonances at normal light incidence (up to approximately 45 in water, 85 in glycerol), which worsen as the period increases and the nanostructures become relatively too small.

At this point we had very good results for collective resonances at a normal angle of incidence in water and glycerol, but we still wanted to improve the resonances in air. Theory and the experimental results of Odom et al. in an index-matched environment[17] suggest that the height of the unit cell nanostructure, not just overall volume, may be especially important for supporting resonances at normal light incidence.

dx.doi.org/10.1021/ph5002186 | ACS Photonics 2014, 1, 1116–1126

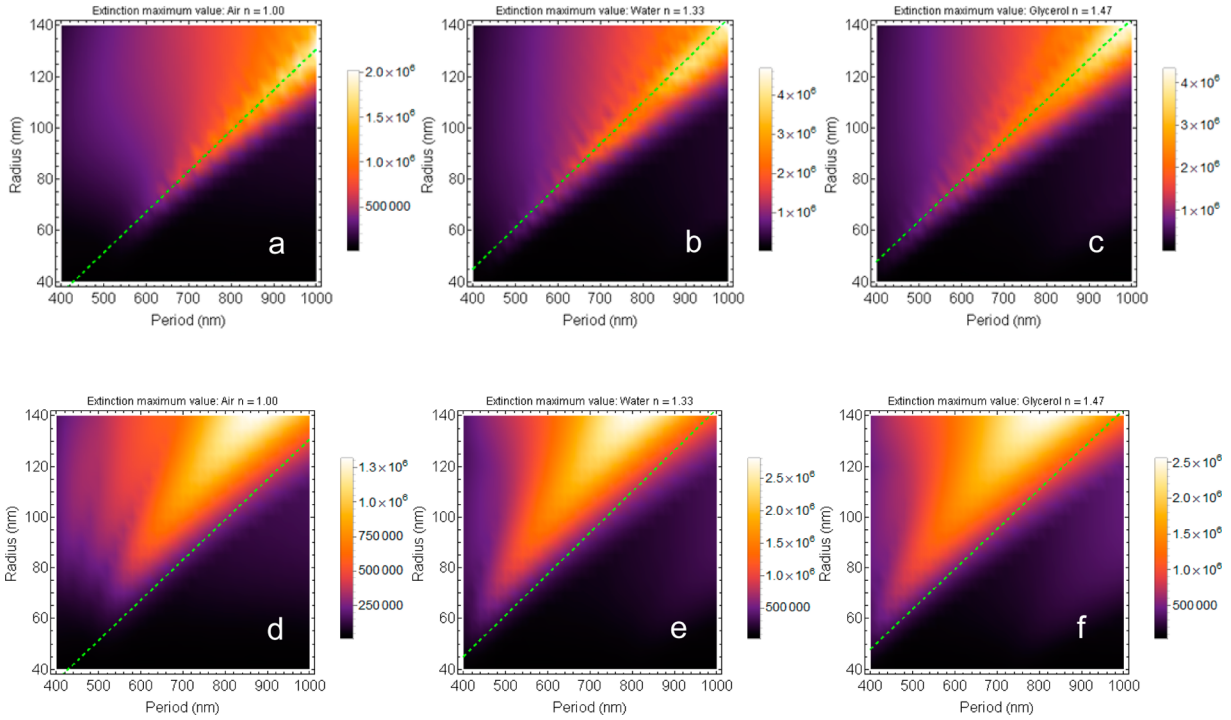

Figure 6. Simulation of the extinction maximum values produced by various combinations of the array period and nanostructure size (spherical nanostructures assumed). (a–c) Prediction of the model for 100 interacting nanoparticles, in air, water, and glycerol, respectively. The green dotted line provides an indication of the optimal combination of structure size and array period. It is clear that a larger than optimal ratio of size to period is predicted to perform better than a smaller than optimal ratio. (d–f) Predictions for 10 particles in air, 13 particles in water, and 15 particles in glycerol, respectively. Here the number of particles has been reduced to an effective value to account for the effects of spatial decoherence. The positions of the green lines are unchanged, indicating a shift of the optimum ratio toward larger particles and a broadening of the distribution.

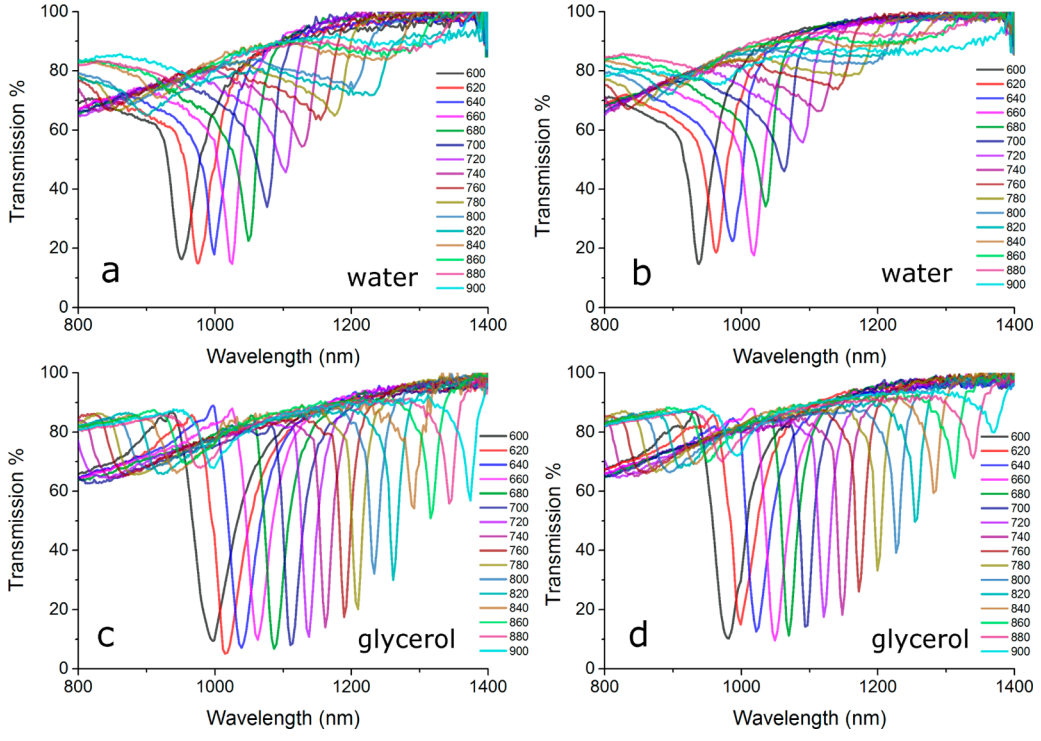

Figure 7. Transmission of arrays of larger, 100 nm tall, square nanostructures with periods from 600 to 900 nm. (a) Structures 210 nm square in water, (b) structures 195 nm square in water, (c) structures 210 nm square in glycerol, (d) structures 195 nm square in glycerol. Clearly there are many samples with high quality factor resonances.

While we had made the nanostructures larger, they were still only 100 nm tall and a poor approximation of the spheres for which we have calculated our theoretical predictions. To this end, we fabricated arrays of nanocubes with sizes around 200

dx.doi.org/10.1021/ph5002186 | ACS Photonics 2014, 1, 1116–1126

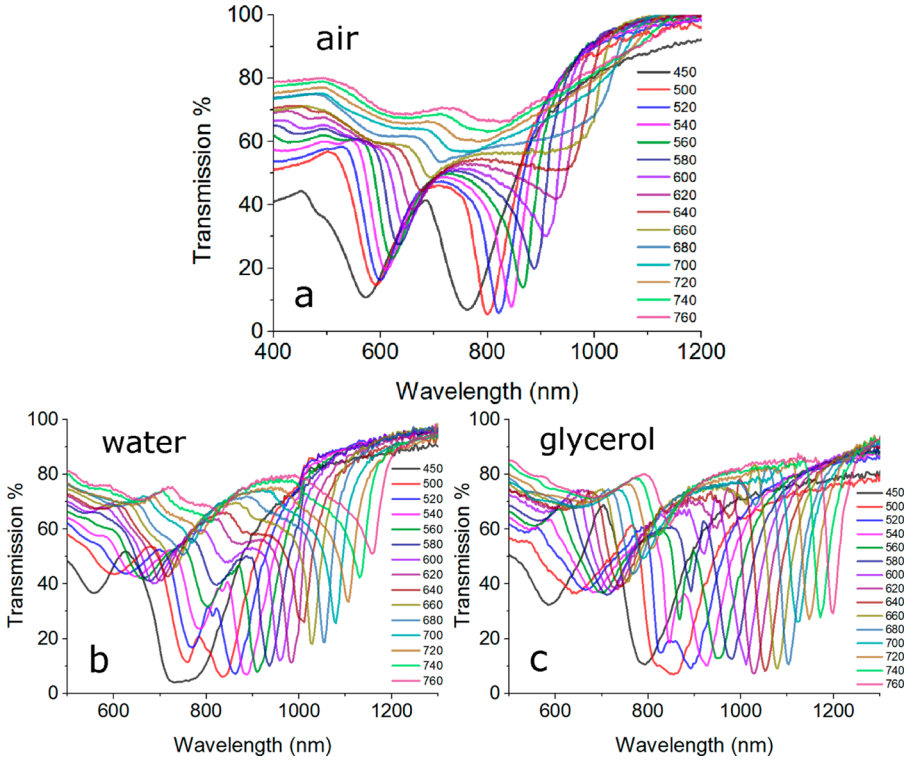

Figure 8. Transmission of arrays of even larger, 200 nm tall, square nanostructures, with periods varying from 450 to 760 nm. Data presented are from structures 200 × 200 × 200 nm in size. (a) In air, (b) in water, and (c) in glycerol.

nm × 200 nm (in-plane) and height 200 nm (out-of-plane). The experimental results for these structures are shown in Figure 8. The collective resonances observed at normal light incidence for these taller structures followed theoretical predictions and showed resonances with high quality factors up to 19 in air.

It is important to note that transmission spectra were measured with focusing optics, using lenses of numerical aperture 0.1 (see Methods). The presence of the focusing optics was a practical necessity, because of the restrictions on sample array size from the electron beam fabrication time involved. The higher numerical aperture implies a lower degree of spatial coherence, which in turn reduces the resonance quality factor (due to reduction of a number of nanostructures that vibrate in phase and hence are effectively involved in the production of diffracted orders). Resonance quality factors would be expected to be even higher in the case of collimated illumination. The effect of the focusing optics on the optimum resonance conditions can be seen in Figure 6d–f. Since we present these results with their practical application in mind, the presence of focusing optics is a realistic representation of the optical setup that would be used in a biosensing application, and thus is appropriate.

In summary, our highest approximate quality factors ($Q = \lambda/\mathrm{fwhm}$) measured in each environment are 19 in air ($n = 1.00$, $\lambda = 843$ nm, period $a = 540$ nm, structures 200 × 200 × 200 nm), 45 in water ($n = 1.31$, $\lambda = 1025$ nm, $a = 660$ nm, structures 195 × 195 × 100 nm), and 85 in glycerol ($n = 1.44$, $\lambda = 1228$ nm, $a = 800$ nm, structures 200 × 200 × 100 nm). We have achieved these results with arrays of L-shaped and square nanostructures for biosensing applications and tall square nanostructures for chemical applications in air.

THEORY

The results obtained in our work can be explained qualitatively (and sometimes even quantitatively) with the help of a coupled dipole approximation. The analysis in this section is similar in spirit to studies of the model by Markel[23,25] and Schatz.[24,26] Consider an ordered array of particles on a flat substrate illuminated by a collimated light at some angle of incidence. The response of an array can be described by effective polarizability:

$$\alpha_{\mathrm{eff}} = \frac{1}{1/\alpha - S} \tag{1}$$

where α is the polarizability of a single particle and S is the corresponding retarded dipole sum. The collective (diffraction-coupled) resonance happens when $\mathrm{Re}(1/\alpha - S) = 0$ or when $\mathrm{Re}(1/\alpha - S)$ is minimal. Figures 9 and 10 show the behavior of the corresponding functions for a regular 1D array of 100 gold spheres of radius r in an asymmetric (air–glass interface) or a symmetric case (in the air). We performed calculations in 1D for the sake of simplicity: our conclusions are based on topological considerations and will hold in the 2D case as well. The nature of the diffractive coupled plasmonic resonance is hiding in the behavior of the inverse polarizability and the dipole sum S. The real part of the dipole sum shows spikes at the Rayleigh anomaly wavelengths (which correspond to the disappearance of a diffractive order),[13] while the imaginary part of S shows step-like jumps at the Rayleigh wavelengths corresponding to Wood anomalies. (The first Rayleigh wavelength in the ambient medium with refractive index n is given by $\lambda_1 = a(n + \sin\theta)$, and the first substrate Rayleigh wavelength is given by $\lambda_{s1} = a(n_s + \sin\theta)$, where n_s is the substrate refractive index and a the array period. The spikes in $\mathrm{Re}(S)$ at these wavelengths would diverge in an infinite array,[26]

dx.doi.org/10.1021/ph5002186 | ACS Photonics 2014, 1, 1116–1126

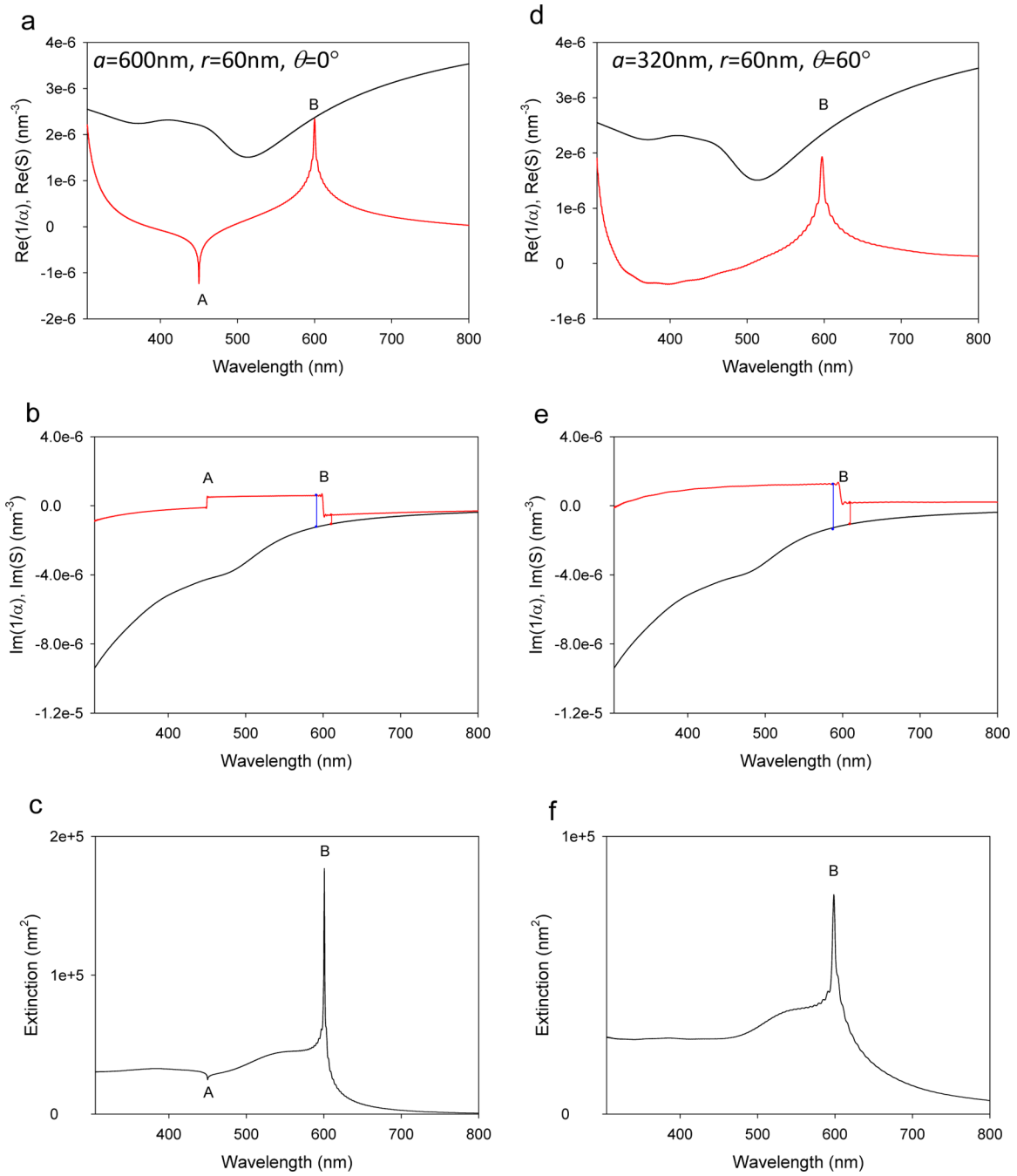

Figure 9. Spectral behavior of inverse susceptibility of gold nanospheres $1/\alpha$ (black), dipole sum S (red), and corresponding extinction for 100 interacting nanostructures with parameters as follows: (a–c) period a = 600 nm, r = 60 nm at normal incidence (glass substrate); (d–f) period a = 320 nm, r = 60 nm, θ = 60°, air.

but in a finite array they are constrained and broadened. Our sample arrays were 100 or 200 μm square in size. As a result, focusing optics were required to practically illuminate the samples. Focusing optics result in a finite spatial coherence length of the incident beam of about λ/NA, where NA is the numerical aperture of the lens, which is akin to limiting the number of nanoparticles that oscillate in phase and participate in the collective resonance, further broadening the resonances.)

The magnitude of the dipole sum S and the inverse polarizability $1/\alpha$ depend on the array period a and the size of the particle, respectively, as well as on the refractive indices of all media involved, such as ambient medium, substrate, and the metal from which the nanoparticles are made. It is the interplay between real and imaginary parts of the inverse polarizability and the dipole sum S that defines the shape of the resonances. There are two basic scenarios for the collective resonances.

Case I: Near the resonance, the real part of $1/\alpha$ is larger than the real part of the dipole sum S. In this case, the diffractive coupled resonance is observed very close to the Rayleigh wavelength, where the difference $\mathrm{Re}(1/\alpha - S)$ becomes minimal. Since the difference in imaginary part $\mathrm{Im}(1/\alpha - S)$ shows a step-like jump at the Rayleigh wavelength, the resonance demonstrates an asymmetric shape with a well-defined cutoff at the Rayleigh wavelength. Figure 9a presents $\mathrm{Re}(1/\alpha)$ and $\mathrm{Re}(S)$ in case I, calculated for an array of spherical

dx.doi.org/10.1021/ph5002186 | ACS Photonics 2014, 1, 1116–1126

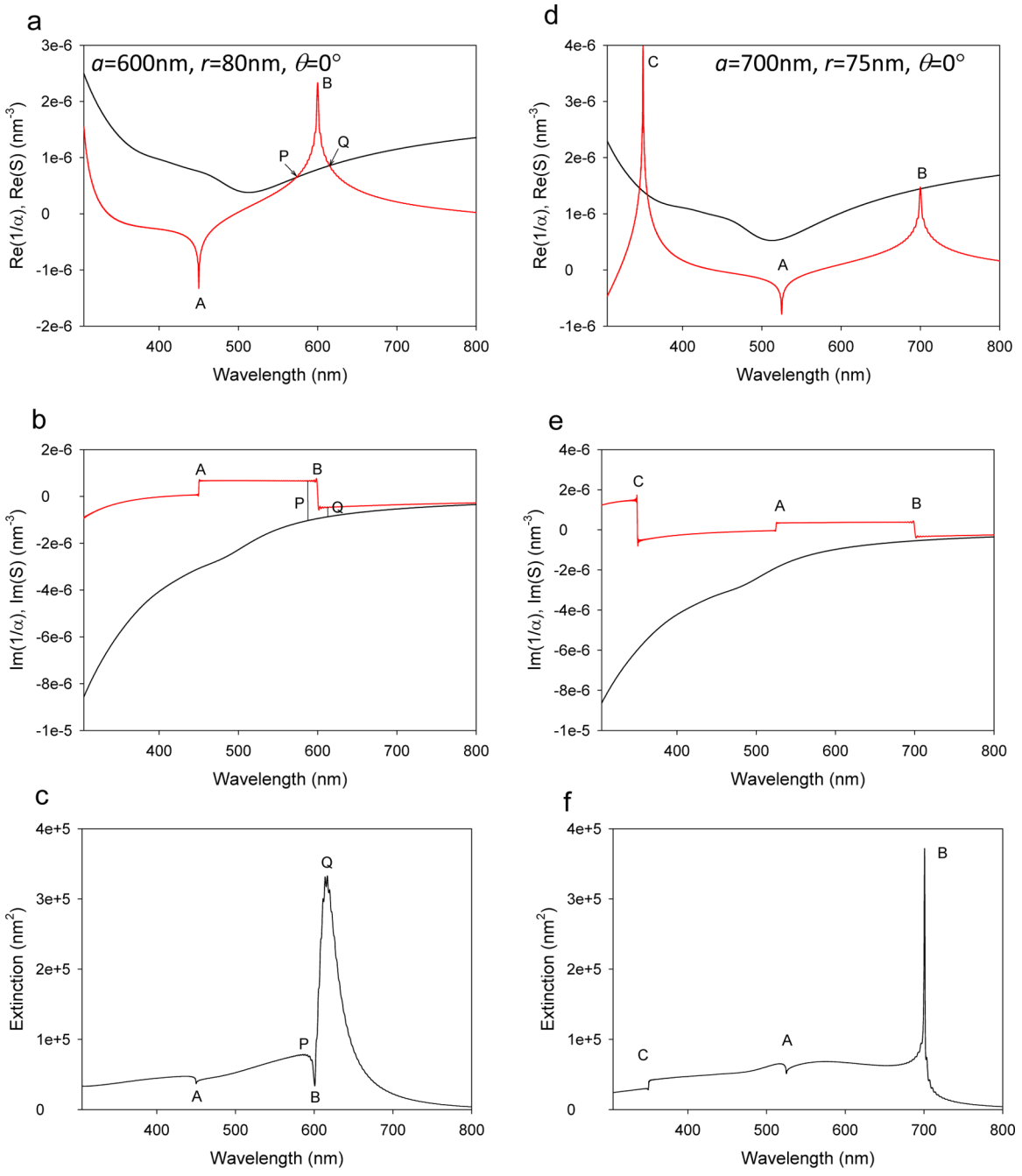

Figure 10. Spectral behavior of inverse susceptibility of gold nanospheres $1/\alpha$ (black), dipole sum S (red), and corresponding extinction calculated at normal incidence for 100 interacting nanostructures on a glass substrate: (a–c) period a = 600 nm, r = 80 nm; (d–f) period a = 700 nm, r = 75 nm, θ = 0°, air.

gold particles of period a = 600 nm and radius r = 60 nm at the normal angle of incidence. A and B label Rayleigh wavelengths for the Wood anomaly in the substrate and in air, respectively. The parameters of the array are chosen in such a way that the real part of the diffractive sum S almost touches the real part of inverse polarizability, resulting in $\mathrm{Re}(1/\alpha - S) = 0$ at the position of the Wood anomaly. This means that the effective susceptibility (1) of a nanoparticle at the resonance position is given by the difference in the imaginary parts of S and $1/\alpha$, which are shown in Figure 9b. The difference between $\mathrm{Im}(1/\alpha)$ and $\mathrm{Im}(S)$ is large from the blue side of the resonance and is small from the red part of the resonance; compare blue and red line segments in Figure 9b. This leads to a characteristic asymmetric shape of the resonance shown in Figure 9c.

The magnitude of the dipole sum S decreases with the increase of angle of incidence. As a result, case I is often realized for oblique illumination, where the diffractive coupled resonances are indeed observed very close to the Rayleigh wavelengths.[13] Figure 9d–f provides an example of this situation for an array of spheres with radius r = 60 nm, period a = 320 nm, and angle of incidence 60°. Figure 9d shows $\mathrm{Re}(1/\alpha)$ and $\mathrm{Re}(S)$, Figure 9e shows $\mathrm{Im}(1/\alpha)$ and $\mathrm{Im}(S)$, and Figure 9f gives extinction of the array. We see that the difference between $\mathrm{Re}(1/\alpha)$ and $\mathrm{Re}(S)$ is minimal at the Rayleigh wavelength, while the difference between $\mathrm{Im}(1/\alpha)$ and $\mathrm{Im}(S)$ is

dx.doi.org/10.1021/ph5002186 | ACS Photonics 2014, 1, 1116–1126

again large from the blue side of the resonance and is small from the red part of the resonance (blue and red line segments in Figure 9e), which leads to an asymmetric shape of the resonance, Figure 9f.

Case II: At the resonance region, the real part of $1/\alpha$ is smaller than the real part of the dipole sum S, and they intersect each other; see Figure 10a. In this case, we have two spectral points P and Q where $\mathrm{Re}(1/\alpha - S) = 0$, which corresponds to the collective resonances near the Rayleigh wavelength represented by the spectral point B. (Point A corresponds to the Rayleigh wavelength in the substrate.) The spectral point B (the Rayleigh wavelengths in ambient medium) in case II corresponds to the minimum of the extinction, Figure 10f, due to the fact that the difference $\mathrm{Re}(1/\alpha - S)$ is large at this point. (This behavior could be reverted after the Brewster angle.) The points P and Q where $\mathrm{Re}(1/\alpha - S) = 0$ both correspond to the diffractive coupled resonances. However, the strengths of the resonances for P and Q (and excited electric fields) are different due to different magnitudes of the imaginary part of $1/\alpha - S$. Indeed, $\mathrm{Im}(1/\alpha - S)$ is much larger on the blue part of the Wood anomaly than on the red part (compare blue and red line segments in Figure 10b), which leads to much more pronounced resonance at longer wavelength in the point Q rather than in the spectral point P, Figure 10c. When comparing with our measured transmission spectra, features such as the predicted extinction minimum at the Rayleigh wavelength, B, appear red-shifted from their calculated positions (e.g., the vertical lines in Figure 5). This is because the anomaly wavelengths marked by lines were calculated as $\lambda_R = na$, where $n = 1.00$ for air, 1.33 for water, and 1.47 for glycerol, and a is the array period. In reality, because the resonances in each nanostructure couple through light scattered in the plane of the array, the environment "seen" by this light not only includes the air, water, or glycerol but also has a significant contribution from the gold of the nanostructures and the glass substrate. Ideally, one would use the formula $\lambda_R = n_{\mathrm{eff}}a$, where n_{eff} is an effective refractive index calculated by effective medium theory, but for the purposes of this discussion it suffices to acknowledge that $n_{\mathrm{eff}} > n$ and is responsible for this red-shift.

This simple analysis suggests that the best resonances (with highest excited fields and narrowest shapes) should be observed for the transition region between case I and case II, where $\mathrm{Re}(1/\alpha)$ touches or just intersects $\mathrm{Re}(S)$ at the Wood anomaly, at the condition of minimal $\mathrm{Im}(1/\alpha - S)$. Therefore, in order to optimize collective resonances for resonance width, we should look for the larger periods (as $\mathrm{Im}(1/\alpha - S)$ decreases with the wavelength) and choose larger sizes of nanoparticles (to guarantee case I). Figure 10d and e represent this ideal scenario observed for $a = 700$ nm, $r = 75$ nm at a normal angle of incidence. It is worth noting that the theoretical quality of this resonance can be evaluated as $Q = 700$.

The condition of optimal field enhancement is also observed for the resonances at the transition region between case I and case II. The field enhancement Γ can be evaluated from the dipole moment of the nanoparticle, $p = \alpha_{\mathrm{eff}}E_0 = (1/(1/\alpha - S))E_0$, which yields

$$\Gamma = \left| \left(\frac{2\pi}{\lambda}\right)^2 \frac{\alpha}{r(1 - \alpha S)} \right|$$

where λ is the wavelength of the light. The field enhancement ratio will be maximal for larger periods and sizes of nanoparticles that provide intersection of $\mathrm{Re}(1/\alpha)$ and $\mathrm{Re}(S)$ close to the case I resonances. For example, $\Gamma = 7.1$ for $a = 700$ nm and $r = 81$ nm and $\Gamma = 8.5$ for $a = 900$ nm and $r = 108$ nm.

DISCUSSION

It is common to calculate figure of merits (FOMs) to quantify the sensing potential of plasmon resonances.[27,28] One is typically defined as the change in a measured quantity (such as the wavelength of the resonance minimum) per refractive index unit (this quantity is termed the "sensitivity", S) and is usually normalized to give the FOM by dividing by the fwhm of the resonance dip (a sharper peak gives a more precise indication of the resonance minimum position). This FOM adequately quantifies the sensing potential of plasmonic modes in configurations similar to those used in commercial instruments, where the angular shift of a single resonance minimum at a steep angle of incidence is used to detect a change in refractive index at the surface. However, for our purposes this FOM is problematic for a number of reasons. Our structures exhibit complex resonances that do not fit a Lorentzian profile, making the assignment of a value of the fwhm to each peak a difficult and subjective exercise. Where quality factors have been quoted, peak height for the fwhm was measured approximately from the left-hand (low-wavelength) "shoulder" of the resonance dip to the resonance minimum, and thus the values must be considered estimates for this reason. Additionally, this FOM may also not be the most appropriate way of quantifying the sensing potential in a simplified biosensing setup at normal incidence.

Similar considerations prompted Becker et al.[29] to define an alternative figure-of-merit (FOM*) for LSPR resonances, where $\mathrm{FOM}^* = ((\mathrm{d}I/\mathrm{d}n)/I)_{\max}$.[29] This FOM* is a more appropriate choice for our purposes. The simplified biosensing application that we propose for our structures would involve measuring changes in intensity in transmission, possibly with a laser at one wavelength, which could be chosen to achieve the maximum FOM*. This definition avoids the need to assign a subjective fwhm to each peak.

All samples were measured at six different refractive indices from 1.31 to 1.44 (measured in the wavelength range 800–1400 nm; see Methods) and the sensitivities, FOM, and FOM* calculated accordingly. Calculated sensitivities were mostly around 300 nm/RIU, reaching 380 nm/RIU for structures 200 × 200 × 200 nm with a period 600 nm. This corresponds to a FOM of approximately 13.

Our highest measured FOM* was 120 at 732 nm, for the sample with structures 210 × 210 × 200 nm in size and array period 450 nm (Figure 11). We measured FOM*s better than 40 up to detection wavelengths of 1000 nm. Interestingly, the highest FOM*s measured were not always for peaks with the highest estimated quality factor; rather they were often for wider, asymmetrical peaks where one side of a peak varied rapidly with changing refractive index, as in Figure 11. This highlights the unsuitability of the quality factor and the "traditional" FOM for quantification of array biosensing potential in this configuration.

CONCLUSION

We have fabricated nanoplasmonic arrays supporting collective, diffraction-coupled resonances that can be excited with light at a normal angle of incidence in asymmetric air and water environments. The nanostructure and array geometries were

dx.doi.org/10.1021/ph5002186 | ACS Photonics 2014, 1, 1116–1126

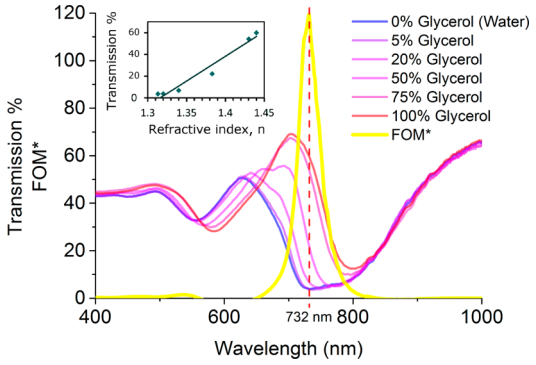

Figure 11. Transmission variation with refractive index and FOM* variation with wavelength for the sample with the highest measured FOM* of 120. Sample structures 210 × 210 × 200 nm in size and array period 450 nm. Inset: Linear fit at the 732 nm peak of the FOM*.

optimized for their bio- and chemical sensing potential by several stages of experimental and theoretical investigation. We have made samples with a very high FOM* (up to 120 in water) for biosensing applications over a range of wavelengths from 700 to 1000 nm (FOM* from 40−120), as well as resonances of unusually high quality in air ($Q \approx 19$) and water ($Q \approx 45$). The high figure of merit and potential for simpler fabrication, coupled with the fact that the resonances were excited with focusing optics at normal incidence, make these structures well suited for greatly simplified sensing applications.

METHODS

Samples were fabricated by electron beam lithography. First, a 1.2 mm thick glass substrate was coated with 3 nm of chromium to prevent charging. All except the 200 nm tall structures were made using a bilayer PMMA resist; first 495k, 2%, spun at 3000 rpm and then 950k, 3%, spun at 5000 rpm and baked for 15 min after each spin-coating step. For the 200 nm tall structures, the first layer was duplicated. Gold was then evaporated onto the sample by electron beam before lift-off. Finally, the chromium was chemically etched from the surface of the sample, except for the area underneath the gold structures.

Transmission and ellipsometric spectra were measured with a focusing beam ellipsometer (T.A. Woollam Co. Inc. M-2000F). The lenses used had numerical aperture 0.1. The light source was a xenon lamp, and the measurement wavelength range was 300−1700 nm. Transmission through the arrays was normalized to transmission through the plain glass substrate. For quantification of the biosensing potential via the FOM and FOM*, all samples were measured at six different concentrations of glycerol solution in water, 0% (pure water), 5%, 20%, 50%, 75%, and 100% (pure glycerol), which were measured to have refractive indices of 1.31, 1.32, 1.34, 1.38, 1.43, and 1.44, respectively, in the wavelength range 800−1400 nm containing the resonance minima, varying by <1% over this range. The water/glycerol solutions and the sample were contained in a glass cuvette between the focusing optics. The FOM was estimated, and the FOM* calculated using a linear fit for $d\lambda/dn$ and dI/dn and dividing by I for pure water.

AUTHOR INFORMATION

Corresponding Author

*E-mail: benjamin.thackray@postgrad.manchester.ac.uk.

Notes

The authors declare no competing financial interest.

ACKNOWLEDGMENTS

The work has been supported by EPSRC grant EP/K011022/1 and Samsung grant SAIT GRO.

REFERENCES

(1) Lee, H. J.; Nedelkov, D.; Corn, R. M. Surface plasmon resonance imaging measurements of antibody arrays for the multiplexed detection of low molecular weight protein biomarkers. *Anal. Chem.* **2006**, *78*, 6504−6510.

(2) Gobi, K. V.; Iwasaka, H.; Miura, N. Self-assembled PEG monolayer based SPR immunosensor for label-free detection of insulin. *Biosens. Bioelectron.* **2007**, *22*, 1382−1389.

(3) Mannelli, I.; Minunni, M.; Tombelli, S.; Wang, R.; Michela Spiriti, M.; Mascini, M. Direct immobilisation of DNA probes for the development of affinity biosensors. *Bioelectrochemistry* **2005**, *66*, 129−138.

(4) Luong, J. H. T.; Male, K. B.; Glennon, J. D. Biosensor technology: Technology push versus market pull. *Biotechnol. Adv.* **2008**, *26*, 492−500.

(5) Rich, R. L.; Myszka, D. G. Grading the commercial optical biosensor literature—Class of 2008: 'the mighty binders'. *J. Mol. Recognit.* **2010**, *23*, 1−64.

(6) Tang, Y.; Zeng, X.; Liang, J. Surface plasmon resonance: An introduction to a surface spectroscopy technique. *J. Chem. Educ.* **2010**, *87*, 742−746.

(7) Anker, J. N.; Hall, W. P.; Lyandres, O.; Shah, N. C.; Zhao, J.; Van Duyne, R. P. Biosensing with plasmonic nanosensors. *Nat. Mater.* **2008**, *7*, 442−453.

(8) Haes, A. J.; Chang, L.; Klein, W. L.; Van Duyne, R. P. Detection of a biomarker for Alzheimer's disease from synthetic and clinical samples using a nanoscale optical biosensor. *J. Am. Chem. Soc.* **2005**, *127*, 2264−2271.

(9) Willets, K. A.; Van Duyne, R. P. Localized surface plasmon resonance spectroscopy and sensing. *Annu. Rev. Phys. Chem.* **2007**, *58*, 267−297.

(10) Kabashin, A. V.; Patskovsky, S.; Grigorenko, A. N. Phase and amplitude sensitivities in surface plasmon resonance bio and chemical sensing. *Opt. Express* **2009**, *17*, 21191−21204.

(11) Halas, N. J.; Lal, S.; Chang, W.-S.; Link, S.; Nordlander, P. Plasmons in strongly coupled metallic nanostructures. *Chem. Rev.* **2011**, *111*, 3913−3961.

(12) Kravets, V. G.; Schedin, F.; Kabashin, A. V.; Grigorenko, A. N. Sensitivity of collective plasmon modes of gold nanoresonators to local environment. *Opt. Lett.* 35, 956−958.

(13) Kravets, V. G.; Schedin, F.; Grigorenko, A. N. Extremely narrow plasmon resonances based on diffraction coupling of localized plasmons in arrays of metallic nanoparticles. *Phys. Rev. Lett.* **2008**, *101*, 087403.

(14) Auguié, B.; Barnes, W. L. Collective resonances in gold nanoparticle arrays. *Phys. Rev. Lett.* **2008**, *101*, 143902.

(15) Auguié, B.; Bendaña, X. M.; Barnes, W. L.; García de Abajo, F. J. Diffractive arrays of gold nanoparticles near an interface: critical role of the substrate. *Phys. Rev. B* **2010**, *82*, 155447.

(16) Kravets, V. G.; Schedin, F.; Jalil, R.; Britnell, L.; Gorbachev, R. V.; Ansell, D.; Thackray, B.; Novoselov, K. S.; Geim, A. K.; Kabashin, A. V.; Grigorenko, A. N. Singular phase nano-optics in plasmonic metamaterials for label-free single-molecule detection. *Nat. Mater.* **2013**, *12*, 304−309.

(17) Zhou, W.; Odom, T. W. Tunable subradiant lattice plasmons by out-of-plane dipolar interactions. *Nat. Nanotechnol.* **2011**, *6*, 423−427.

(18) Yizhuo, C.; Ethan, S.; Tian, Y.; Kenneth, B. C. Experimental observation of narrow surface plasmon resonances in gold nanoparticle arrays. *Appl. Phys. Lett.* **2008**, *93*, 181108.

(19) Kravets, V. G.; Zoriniants, G.; Burrows, C. P.; Schedin, F.; Geim, A. K.; Barnes, W. L.; Grigorenko, A. N. Composite Au

nanostructures for fluorescence studies in visible light. *Nano Lett.* **2010**, *10*, 874−879.
(20) Kravets, V. G.; Zoriniants, G.; Burrows, C. P.; Schedin, F.; Casiraghi, C.; Klar, P.; Geim, A. K.; Barnes, W. L.; Grigorenko, A. N. Cascaded optical field enhancement in composite plasmonic nanostructures. *Phys. Rev. Lett.* **2010**, *105*, 246806.
(21) Kravets, V. G.; Schedin, F.; Grigorenko, A. N. Fine structure constant and quantized optical transparency of plasmonic nanoarrays. *Nat. Commun.* **2012**, *3*, 640.
(22) Thackray, B.; Kravets, V. G.; Schedin, F.; Jalil, R.; Grigorenko, A. N. Resistive coupling of localized plasmon resonances in metallic nanostripes through a graphene layer. *J. Opt. (Bristol, U.K.)* **2013**, *15*, 114002.
(23) Markel, V. A. Coupled-dipole approach to scattering of light from a one-dimensional periodic dipole structure. *J. Mod. Opt.* **1993**, *40*, 2281−2291.
(24) Zou, S.; Janel, N.; Schatz, G. C. Silver nanoparticle array structures that produce remarkably narrow plasmon lineshapes. *J. Chem. Phys.* **2004**, *120*, 10871−10875.
(25) Markel, V. A. Divergence of dipole sums and the nature of non-Lorentzian exponentially narrow resonances in one-dimensional periodic arrays of nanospheres. *J. Phys. B: At., Mol. Opt. Phys.* **2005**, *38*, L115.
(26) Shengli, Z.; George, C. S. Theoretical studies of plasmon resonances in one-dimensional nanoparticle chains: narrow lineshapes with tunable widths. *Nanotechnology* **2006**, *17*, 2813.
(27) Offermans, P.; Schaafsma, M. C.; Rodriguez, S. R. K.; Zhang, Y.; Crego-Calama, M.; Brongersma, S. H.; Gómez Rivas, J., Universal scaling of the figure of merit of plasmonic sensors. *ACS Nano* **2011**, *5*, 5151−5157.
(28) Ye, J.; Van Dorpe, P. Improvement of figure of merit for gold nanobar array plasmonic sensors. *Plasmonics* **2011**, *6*, 665−671.
(29) Becker, J.; Trügler, A.; Jakab, A.; Hohenester, U.; Sönnichsen, C. The optimal aspect ratio of gold nanorods for plasmonic bio-sensing. *Plasmonics* **2010**, *5*, 161−167.